

Dynamic phase diagram of plastically deformed amorphous solids at finite temperature

Daniel Korchinski^{*} and Jörg Rottler

Department of Physics and Astronomy and Stewart Blusson Quantum Matter Institute,
University of British Columbia, Vancouver BC V6T 1Z1, Canada



(Received 12 April 2022; revised 22 June 2022; accepted 27 July 2022; published 6 September 2022)

The yielding transition that occurs in amorphous solids under athermal quasistatic deformation has been the subject of many theoretical and computational studies. Here, we extend this analysis to include thermal effects at finite shear rate, focusing on how temperature alters avalanches. We derive a nonequilibrium phase diagram capturing how temperature and strain rate effects compete, when avalanches overlap, and whether finite-size effects dominate over temperature effects. The predictions are tested through simulations of an elastoplastic model in two dimensions and in a mean-field approximation. We find a scaling for temperature-dependent softening in the low-strain rate regime when avalanches do not overlap, and a temperature-dependent Herschel-Bulkley exponent in the high-strain rate regime when avalanches do overlap.

DOI: [10.1103/PhysRevE.106.034103](https://doi.org/10.1103/PhysRevE.106.034103)

I. INTRODUCTION

Amorphous solids are materials that, like fluids, lack long-range order on the constituent particle scale, yet are solid at rest. When deformed slowly, these solids respond, first seemingly elastically and then, once a critical stress is achieved, plastically [1,2]. This response can be either brittle, with system spanning shear bands, or ductile, with homogeneous plasticity [2–5]. Ductile plastic flow is “jerky,” with periods of elastic stress-loading punctuated by short bursts of stress-releasing plastic rearrangement dubbed “avalanches.” These avalanches can be decomposed into individual shear transformations (STs), regions of plastic deformation typically involving a few tens of particles [6–8]. Each ST causes a rearrangement that locally relieves stress, while inducing a long-range a quadrupolar stress field [8–11] that can trigger further STs in an avalanche. In the flowing state, in the absence of flow inhomogeneities, the hallmarks of a dynamical phase transition emerge: avalanches are scale free, with non-trivial critical exponents [12–20].

Much theoretical attention has been paid to the ductile yielding transition in the athermal and quasistatic (AQS) limit [12,16,19–22]. This limit is appropriate when the plastic ST timescale τ , over which rearrangements occur, is much smaller than the periods of elastic loading (set by the driving rate) and the timescale of thermally triggered STs. When the driving rate competes with the timescale of plastic rearrangements, rheological effects begin to alter the phase-transition picture [23–26]. For systems where the constituent particles are large and Brownian motion is small (e.g., foams, emulsions, dense suspensions, etc.), thermal effects can be safely neglected [27]. However, for systems with smaller particles or higher temperatures (e.g., metallic glasses close to the

glass-transition temperature T_g), thermal effects begin to play a role [2].

Thermal history and preparation can affect whether yielding is brittle or ductile [2,5,28–30]. Specifically in a ductile steady-state flow, the competition of thermal and driving-rate timescales changes the rheology as follows: If driving rates $\dot{\gamma}$ are increased, so that the loading time between avalanches becomes so short as to be comparable to the duration of the average avalanche $\langle t \rangle_{av}$, avalanches begin to overlap temporally, as shown for instance in the molecular dynamics study of Karmarkar *et al.* [31]. These overlapping avalanches destroy the anomalous stress fluctuations of the AQS yielding transition, and the flow stress Σ rises above the athermal critical stress Σ_c according to the Herschel-Bulkley (HB) law [12,32,33],

$$\Sigma(T = 0, \dot{\gamma}) = \Sigma_c + A\dot{\gamma}^n, \quad (1)$$

where n is the Herschel-Bulkley exponent and $T = 0$ indicates the athermal limit. If Eq. (1) is formulated as a critical scaling law $(\Sigma - \Sigma_c)^\beta \sim \dot{\gamma}$, then $\beta = 1/n$ can be viewed as an order parameter exponent, in analogy to static critical phenomena.

In overdamped systems in general, the flow stress decreases with temperature and increases with driving rate. Computational studies of thermal activation effects on the yielding transition have been conducted with molecular dynamics simulations of glass formers [34] and, more recently, with mesoscale elastoplastic models (EPMs) [35–37]. While molecular dynamics simulations simulate each atom (or molecule), EPMs coarse grain to the level of elastic blocks. These blocks fluidize once the local stress exceeds a threshold, whereupon they plastically dissipate the local stress. The advantage of this coarse graining is that one can simulate large systems for long times, while respecting the underlying symmetries of the yielding transition. Recent EPM studies have mostly focused on the scaling of the flow stress and have proposed that it takes a scaling form [35,36] (in analogy with

*djkorchi@phas.ubc.ca

the depinning transition [38]),

$$\dot{\gamma} \sim T^\psi f\left(\frac{\Sigma(T, \dot{\gamma}) - \Sigma_c}{T^{1/\alpha}}\right), \quad (2)$$

where $\psi = \beta/\alpha$ is the Fisher thermal rounding exponent, and α is an exponent that characterizes the shape of the energy landscape (see below).

Relatively little work has focused on the interplay between temperature effects and the scaling description for avalanches. Karmakar *et al.* also showed that like with higher driving rates, increased temperatures interfere with avalanches, destroying their anomalous scaling with system size [31]. In that work, the stress-fluctuation scales can be worked out by determining the timescales of the system and identifying when they compete with each other.

Subsequent to that work, there have been significant theoretical developments in the AQS regime, with scaling theories connecting different scale-free aspects of the yielding transition. One useful advance has been the notion of “residual stress” $x = \sigma_{\text{th}} - \sigma$, i.e., the stress necessary to trigger an ST with a threshold σ_{th} in a particular region of the amorphous solid. The distribution of residual stresses $p(x) \sim x^\theta$ is scale free in the thermodynamic limit [12] and plays a key role in driving the anomalous stress fluctuations in these systems. Mesoscale modeling has been particularly helpful in exploring scaling aspects of the yielding transition, as it coarse grains at the level of STs and directly exposes $p(x)$ [21].

To that end, in this work we will use a mesoscale model with Arrhenius activation rule (as in Refs. [35–37]),

$$\lambda(x) = \frac{1}{\tau} \exp\left(-\frac{x^\alpha}{T}\right), \quad (3)$$

to describe the temperature and rate effects on the critical behavior of the yielding transition. This choice of activation rule is motivated by an energy landscape picture: local regions of the amorphous solid are stable because there is an energy barrier (scaling as $U \sim Cx^\alpha$) preventing their rearrangement (with catastrophe theory suggesting $\alpha = 1.5$ [39]). Transition state theory suggests that temperature T causes repeated attempts at crossing these barriers, which succeed at a rate proportional to $\exp[-U(x)/k_B T]$ [40]. In this work, we set $C/k_B = 1$ and the prefactor τ^{-1} is set so that when $x = 0$ (i.e., no barrier), sites activate on average after τ , thus matching the microscopic timescale for ST rearrangement. We match these two timescales because the exponential prefactor in Eq. (3) is the attempt frequency for barrier crossing. In particle scale simulations of model glasses, this attempt frequency is of the order of the atomic vibrational frequency, $f_{\text{vib}} \approx \mathcal{O}(1/\tau)$, while the time taken for a plastic rearrangement is of the same order [41].

With the thermal timescale established, we begin by enumerating the other natural timescales in sheared amorphous solids:

(i) The plastic ST timescale τ over which atomistic rearrangements occur, i.e., the length of time for which a given ST is fluid and the timescale over which stress is dissipated.

(ii) For a site a distance x from instability, the thermal Arrhenius activation timescale $1/\lambda(x) = \tau \exp(x^\alpha/T)$. In this description, sites with residual stress x have a potential barrier to thermal activation scaling as $U \sim x^\alpha$.

(iii) For a site a distance x from instability, the mechanical yielding timescale $x/\mu\dot{\gamma}$, with μ a shear modulus.

(iv) The average avalanche duration $\langle t \rangle_{\text{av}}$.

(v) The average loading time between triggering avalanches $\langle t_{\text{load}} \rangle$.

We will use the competition of these timescales to sketch out a phase diagram and predict the scaling in different regimes. Then, using numerical simulations, we will confirm the existence of the different phases and verify the scaling laws present in each phase.

II. THERMALLY ACTIVATED ELASTOPLASTIC MODEL

We use a mesoscale elastoplastic model (EPM), which coarse grains the amorphous solid to a grid of L^d elastically coupled cells. Each cell i has a yield stress $\sigma_{\text{th},i}$ drawn independently from a Weibull distribution (shape parameter $k = 2$) [42,43] and an initial stress $\sigma_i = 0$. The system is driven at a fixed strain rate $\dot{\gamma}$, which adds stress uniformly to all sites at a global rate $\dot{\sigma} = \mu\dot{\gamma}$. In the following, we set $\mu = 1$. Sites fluidize immediately when their residual stress $x = \sigma_{\text{th},i} - |\sigma_i| \leq 0$. Once fluid, sites remain fluid for 2τ , before again becoming elastic. Fluid sites dissipate stress as $\dot{\sigma}_i \sim -\sigma_i/\tau$. We use a finite-element solver to propagate stresses from fluidized sites, which automatically produces the anisotropic Eshelby-like stress fields characteristic of STs. In contrast to the other thermally activated EPMs [35–37], we use a real-space stress propagator more similar to [17,44]. In some of our simulations, we follow Refs. [16,45] and shuffle the indices of the sites when applying the “kicks” from the fluidized sites and refer to these simulations as “shuffled-kernel” or mean-field (MF) simulations. There are two features that distinguish our model from the EPMs used in Refs. [35–37]. First, we study the system under constant strain rate, as is more typical in MD simulations. This makes it challenging to numerically sample the time to failure for sites with $x \approx 1$, but can be accelerated for $\alpha = 1, 2$, to which we restrict our focus in this work. Second, our EPM implementation does not use periodic boundary conditions. For details on the acceleration algorithm and implementation details, see Appendix A.

III. COMPETITION OF TIMESCALES

Equation (3) implies a characteristic stress scale,

$$x_c = T^{1/\alpha}. \quad (4)$$

The Arrhenius activation rate is of the order of $1/\tau$ when $x \leq x_c(T)$. The first two natural timescales to equate are

$$x_c/\dot{\sigma} = \tau, \quad (5)$$

which sets the mechanical yielding timescale for a site with residual stress x_c to the thermal yielding time for a site at or below x_c . This relation defines the solid diagonal orange (light gray) line,

$$\dot{\sigma}_c(T) \equiv \frac{1}{\tau} T^{1/\alpha}, \quad (6)$$

dividing regions 1 and 5 from 2, 3, and 4 in Fig. 1. For simulations above this orange line with $\dot{\sigma} > \dot{\sigma}_c(T)$, thermal effects are minimal since even sites with $x < x_c$ are driven

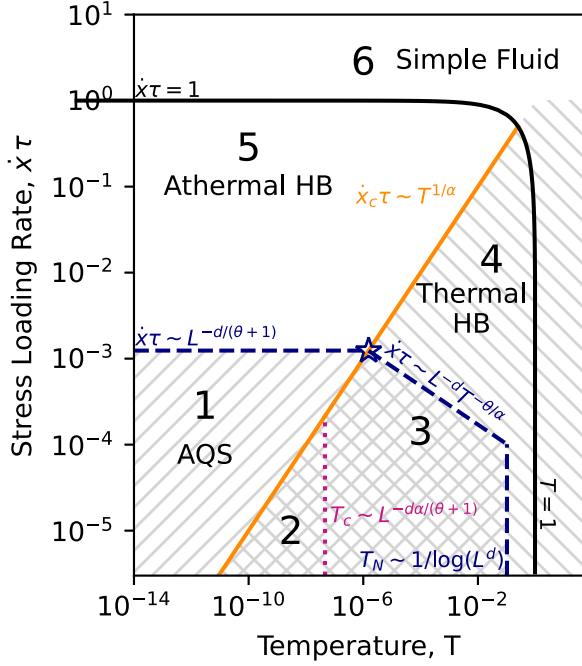


FIG. 1. Dynamical phase diagram for the thermal two-dimensional EPM at $L = 128$ for $\alpha = 2$. The dashed navy (dark gray) line indicates the onset of temporally overlapping avalanches, with the hatching indicating the region with nonoverlapping avalanches. The diagonal solid orange (light gray) line indicates the onset of thermal effects, with hatching indicating that thermal effects are prevalent. The vertical dotted red (gray) line at T_c indicates the onset of thermal truncation of avalanche size. Dashed and dotted lines have finite-size scaling with L .

to mechanical failure at $x = 0$ before thermal activation can occur.

The division between regions 2 and 3 comes from competition between finite-size scaling and the thermal activation of sites. In both regimes, avalanches are scale free up to a cutoff scale, set by the either temperature or the linear dimension L of the system. The size of an avalanche is defined by the stress dissipated by the avalanche, with $S = L^d \delta \Sigma_{av}$ (approximately the number of yielding sites). In the steady state, the average stress dissipated by avalanches must equal the stress loaded between avalanches: $\dot{\gamma} \langle t_{load} \rangle = \langle \delta \Sigma \rangle_{av} = L^{-d} \langle S \rangle$. Since $\langle t_{load} \rangle(L)$ scales with L , this produces a nontrivial scaling for the mean avalanche size $\langle S \rangle$. In the athermal case, an avalanche begins when the weakest site (left at x_{min} by the preceding avalanche) reaches $x = 0$, so in AQS, $\langle t_{load} \rangle \dot{\gamma} = \langle x_{min} \rangle$. If x is independent between sites (which appears to be approximately true), $\langle x_{min} \rangle$ is entirely determined by the probability density function for x , $p(x)$, with $L^{-d} \sim \int_0^{\langle x_{min} \rangle} p(x') dx'$. However, thermal effects alter the form of $p(x)$ from the power-law form $p(x) \sim x^\theta$ expected in the thermodynamic limit.

Arrhenius activations deplete sites with $x < x_c$ (as can be seen in Appendix B, Fig. 10) in the thermal regime. If we approximate the density of sites with $x < x_c$ and $x > 1$ as zero and with $p(x) = Ax^\theta$ for $x \in (x_c, 1)$ elsewhere, and using the

relation $L^{-d} \sim \int_0^{\langle x_{min} \rangle} p(x') dx'$, we obtain

$$\langle x_{min} \rangle \sim \left(\frac{\theta + 1}{A} L^{-d} + x_c^{\theta+1} \right)^{1/(\theta+1)}, \quad (7)$$

which is valid whenever thermal activations occur quickly compared to mechanical yielding (i.e., in regions 2, 3, and 4). Clearly, there is a natural temperature scale when $x_c^{\theta+1} \sim L^{-d}$, i.e., when

$$T_c \sim L^{-d\alpha/(\theta+1)}. \quad (8)$$

This is the vertical red (gray) line dividing regions 2 and 3. The transition across this line is detailed in Sec. IV A, but in essence this phase line captures whether avalanches are truncated by finite size or by nonzero temperature.

At high driving rates, the time needed for amorphous solids to plastically dissipate loaded stress becomes longer than the time needed to trigger a new plastic event, which results in a characteristic shear-thinning stress response, typically captured by the Herschel-Bulkley relation [Eq. (1)]: $\dot{\gamma}^n \sim \Sigma - \Sigma_c$, where $n = 1/\beta$ is the Herschel-Bulkley exponent. This rise in stress above the critical flow stress Σ_c occurs whenever the stress dissipation timescale (be it from avalanches, individual STs, or a more generic dissipative mechanism) competes with the loading timescale. In our case, this first occurs when avalanches (the longest dissipative timescale in our system) begin to temporally overlap, i.e., the loading time is comparable to the duration of avalanches [31].

The next several relations determine the onset of avalanche overlap. We can establish a maximum temperature T_N for which avalanches in a finite-size system remain discrete by setting the rate of activation for L^d freshly injected sites equal to $1/\tau$,

$$\tau^{-1} = \frac{L^d}{\tau} e^{-1^\alpha/T_N}, \quad (9)$$

implying $T_N = 1/\ln(L^d)$. This is the vertical dashed navy (dark gray) line dividing regions 3 and 4 in Fig. 1. At lower temperatures, avalanche overlap can be assisted by higher driving rates. As before, avalanches can overlap because the loading time between avalanches is comparable to the plastic time, i.e.,

$$\langle t_{load} \rangle = \tau.$$

We first handle the thermally assisted case [i.e., $\dot{\gamma} < \dot{\gamma}_c(T)$]. Thermal activation occurs when the weakest site reaches x_c , so the loading time is $\langle t_{load} \rangle = (\langle x_{min} \rangle - x_c)/\dot{\gamma}$. For $T > T_c(L)$, we can expand Eq. (7) to first order in L^{-d} for $\langle x_{min} \rangle$, giving

$$\langle t_{load} \rangle = \frac{1}{\dot{\gamma}} [x_c^{-\theta} L^{-d}]. \quad (10)$$

Using $\langle t_{load} \rangle = \tau$ and $x_c = T^{1/\alpha}$, we find

$$\dot{\gamma}_{overlap}[T > T_c(L)] \sim \frac{1}{\tau} L^{-d} T^{-\theta/\alpha}. \quad (11)$$

This gives the sloped dashed navy (dark gray) line dividing regions 3 and 4 in Fig. 1. Now for the second case, where $\dot{\gamma} > \dot{\gamma}_c(T)$, we know that thermal activation should be rare (i.e., mechanical effects dominate). Then, the form of $p(x)$ is altered to have a size- and drift-velocity-dependent plateau

TABLE I. A summary of the derived phases and scaling of avalanche size or stress with temperature or system size.

No.	Name	Scalings	Notes
1	Athermal quasistatic	$\langle S \rangle_{\text{AQS}} \sim L^{d\theta/(\theta+1)}$	Dynamics are as if $T = 0$ and $\dot{\gamma} = 0$.
2	Finite-size truncated avalanches	$\langle S \rangle \sim L^{d\theta/(\theta+1)} + \mathcal{O}(T^{1/\alpha})$	Minimal temperature effects.
3	Temperature truncated avalanches	$\langle S \rangle \sim T^{-\theta/\alpha}$ $\Sigma_{\text{AQS}} - \langle \Sigma \rangle \sim T^{\theta\sigma/[\alpha(2-\tau)]}$	Avalanche size is truncated by temperature rather than system size.
4	Thermal Herschel-Bulkley	$\langle \Sigma \rangle = \Sigma_c(T) + \dot{\gamma}^{n_{\text{th}}}$	Avalanches overlap, temperature effects present.
5	Athermal Herschel-Bulkley	$\langle \Sigma \rangle = \Sigma_c + \dot{\gamma}^{n_{\text{AQS}}}$	Avalanches overlap, no temperature effects.
6	Simple fluid	$\langle \Sigma \rangle \sim \dot{\gamma}$	Sites yield immediately and independently.

with $p(x) = p_0$ for $x < x_p(\dot{x}, L)$ (see Appendix B, Fig. 10, and associated discussion). If we instead use that $\langle x_{\min} \rangle$ is in the plateau (an appropriate assumption for large L), we have

$$\langle x_{\min} \rangle = L^{-d} p_0^{-1}, \quad (12)$$

where $p_0 = A x_p^\theta$. Then, equating the loading time and the ST plastic time, we have

$$\tau = \langle x_{\min} \rangle / \dot{x}_{\text{overlap}} \sim \frac{L^{-d}}{\dot{x}_{\text{overlap}} x_p(\dot{x}, L)^\theta}, \quad (13)$$

which yields the horizontal dashed navy (dark gray) line, dividing regions 1 and 5. For large L , the onset of the plateau scales as $x_p \sim \tau \dot{x}$, and we have

$$\dot{x}_{\text{overlap}}(T < T_{\text{overlap}}) \sim L^{-d/(1+\theta)}. \quad (14)$$

We have found phase lines [Eqs. (11) and (14)] for avalanche overlap on both sides of the thermal activation phase line \dot{x}_c . These phase lines should be continuous across the thermal activation phase line, meeting at a system-size-dependent temperature T_{overlap} ,

$$L^{-d/(1+\theta)} \sim L^{-d} T_{\text{overlap}}^{-\theta/\alpha} \Rightarrow T_{\text{overlap}} \sim L^{\frac{-d\alpha}{1+\theta}}, \quad (15)$$

which we indicate with the navy (dark gray) star in the phase diagram. Crucially, $T_{\text{overlap}}(L) \sim T_c(L) \sim L^{-d\alpha/(1+\theta)}$, so that the expansion taken in Eq. (10) is always valid. Transitions across these lines are explored in Sec. IV B.

Despite avalanches being ill defined in the thermal and athermal Herschel-Bulkley (HB) phases, we will show numerically in Sec. IV C that the dynamics are still collective since the presence of correlations between sites affects the HB exponent n . At sufficiently high temperature or driving, however, sites yield essentially immediately, destroying any collective effects. When this occurs, the amorphous solid is said to have “fluidized.” In the fluid phase, the stress on any given site i evolves according to $\dot{\sigma}_i = -\sigma_i/\tau + \dot{x}$, which tends to $\sigma_i \rightarrow \tau \dot{x}$. This implies $\langle \Sigma \rangle \sim \dot{\gamma}$, meaning that this phase behaves like a simple Newtonian fluid (hence the name). Fluidization occurs when freshly rejuvenated sites (initially at $x = 1$) in the absence of noise yield within a time of order the mechanical yielding timescale τ . Since sites with $x < x_c(T) = T^{1/\alpha}$ yield within about 1τ , and it takes time $(1 - x_c)/\dot{x}$ for a site initially at $x = 1$ to reach the thermal absorbing barrier, we say that fluidization occurs whenever $\tau \dot{x} > 1 - T^{1/\alpha}$. This gives the line separating athermal and thermal phases (regions 4 and 5) from the fluid phase (region 6). A summarizing table of the derived phases and their pertinent scalings can be found in Table I.

IV. NUMERICAL TESTS OF THE PHASE DIAGRAM

To test our phase diagram and scaling theory, we perform simulations at different stress-loading rates \dot{x} , temperatures T , system sizes L , and with $\alpha = 1$ and $\alpha = 2$, as well as for two-dimensional (2D) simulations and 2D simulations with a shuffled kernel. These shuffled-kernel simulations keep the broad-tailed kick statistics of the 2D simulations, but remove spatial correlations between sites, thus providing a mean-field (MF) realization of the EPM [16]. One consequence of this is that the exponent θ changes from $\theta \approx 0.52$ (in 2D) to $\theta \approx 0.35$, allowing us to vary θ and test scaling relations involving θ . For convenience of the reader, Fig. 2 presents an overview of the regions of the phase diagram that were simulated and indicates the corresponding figures.

A. Avalanche size cutoff

Discrete avalanches exist in regions 1, 2, and 3. In region 1, avalanches do not overlap and thermal activations do not occur, making this the well-studied AQS limit.

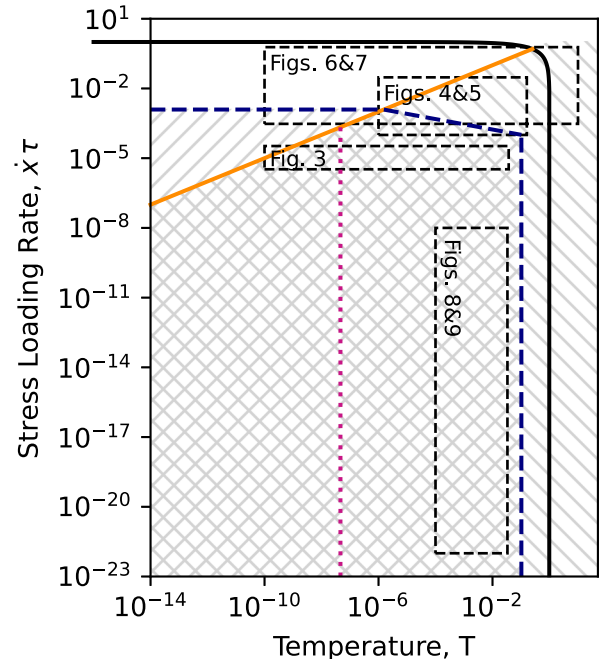


FIG. 2. The phase diagram, as in Fig. 1, but with the regions of phase space explored in different figures marked by rectangles.

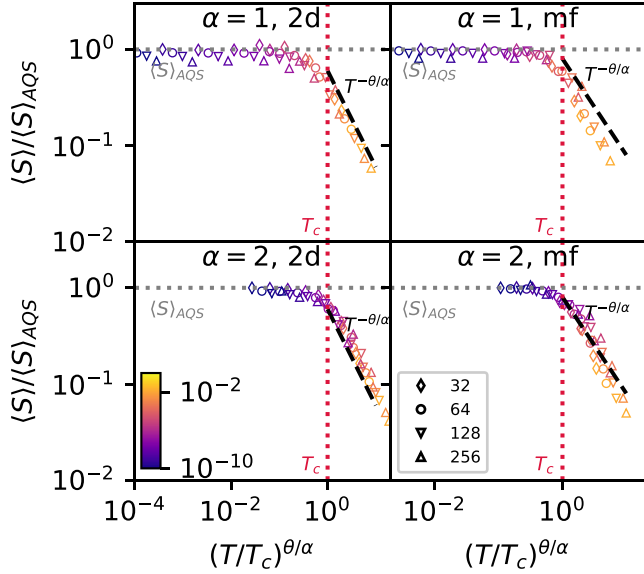


FIG. 3. Rescaled mean avalanche sizes for various temperatures, system sizes, and fixed driving rate $\dot{x}\tau = 10^{-5}$. Lighter colors are hotter temperatures $T \in (10^{-10}, 0.037)$, as indicated in the color bar. Symbols indicate system sizes ranging from $L = 32$ to $L = 256$. $\langle S \rangle_{\text{AQS}}$ scales as $\langle S \rangle_{\text{AQS}} \sim L^{d\theta/(\theta+1)}$ and $T_c \sim L^{-d\alpha/(\theta+1)}$, where $\langle S \rangle = \langle S \rangle_{\text{AQS}}$ and $T = T_c$ are indicated with the dotted lines.

We can study the average avalanche size in regions 1–3 by equating the average stress dissipated in avalanches with the average stress loaded between avalanches. Since avalanche size is defined as $S = L^d \langle \delta \Sigma_{\text{av}} \rangle$, we need merely to compute $\langle \delta \Sigma_{\text{av}} \rangle = \dot{x} \langle t_{\text{load}} \rangle$. In zone 3, where thermal effects are large, we expect $\langle t_{\text{load}} \rangle \sim \frac{1}{\dot{x}} L^{-d} T^{-\theta/\alpha}$ [Eq. (10)], so that

$$\langle S \rangle \sim L^d \dot{x} \langle t_{\text{load}} \rangle \sim T^{-\theta/\alpha} \quad (16)$$

(i.e., no system-size dependence of the mean avalanche size). Meanwhile, for $T \ll T_c$ (i.e., $x_c^{1+\theta} \ll L^{-d}$), Eq. (7) reduces to simply $\langle x_{\text{min}} \rangle \sim L^{-d/(\theta+1)}$. For $\dot{x} \langle t_{\text{load}} \rangle = \langle x_{\text{min}} \rangle - x_c$ with $x_c \ll L^{-d/(1+\theta)}$, we simply have $\langle \delta \Sigma \rangle_{\text{av}} = \dot{x} \langle t_{\text{load}} \rangle = \langle x_{\text{min}} \rangle$. Hence, in the low-temperature limit, $\langle S \rangle_{\text{AQS}} \sim L^{d\theta/(\theta+1)}$.

In Fig. 3, we verify this scaling for $\langle S \rangle$ crossing the 1–2 phase line, plotting $\langle S \rangle / \langle S \rangle_{\text{AQS}}$ against $(T/T_c)^{\theta/\alpha}$, which collapses the AQS plateau and gives a high-temperature tail scaling as $\langle S \rangle \sim [(T/T_c)^{\theta/\alpha}]^{-1}$. These expressions have no driving-rate dependence, and we have verified the crossover and scaling at different driving rates than those shown in Fig. 3. We indeed find almost no driving-rate dependence in the avalanche size, except for those simulations close to T_N (orange in Fig. 3), where lower velocities weakly decrease avalanche size due to stress softening. For this reason, the highest temperatures fall slightly below the $T^{-\theta/\alpha}$ scaling.

Now, assuming a power-law form for the distribution of avalanche sizes $p(S) \sim S^{-\tau} g[S/S_c(T, L)]$, truncated at $S_c(T, L)$ by finite-system size or temperature, we have that

$$\langle S \rangle = \int_0^\infty S^{1-\tau} g(S/S_c) ds = S_c^{2-\tau} \int_0^\infty u^{1-\tau} g(u) du, \quad (17)$$

implying

$$\langle S \rangle \sim S_c^{2-\tau}. \quad (18)$$

Coupled with $\langle S \rangle \sim T^{-\theta/\alpha}$, this implies $S_c(T) \sim T^{-\theta/[\alpha(2-\tau)]}$. Meanwhile, for $T < T_c(L)$, we have the usual AQS regime scaling, $S_c(L) \sim L^{d/[(\theta+1)(2-\tau)]}$, and, consequently, the scaling relation $d_f = d/[(\theta+1)(2-\tau)]$ [21]. Though this scaling relation works well for the shuffled-kernel simulations, we note that for 2D simulations, there are small additional corrections in the AQS limit as described in [46] that we do not account for here. These additional corrections only affect the slow-driving AQS limit since they depend on the structure of the plateau in Fig. 10, which is destroyed by temperature fluctuations.

Our finding, that there are “anomalous” stress fluctuations (i.e., $\langle \delta \Sigma \rangle_{\text{av}} \lesssim L^{-d} = N^{-1}$) below a critical temperature related to the size of the system, and “normal” fluctuations (i.e., $\langle \delta \Sigma \rangle_{\text{av}} \sim L^{-d} \sim N^{-1}$) above this temperature, is consistent with the previous results obtained by Karmakar *et al.* with particle scale simulations [31,47].

B. Avalanche overlap onset

The onset of Herschel-Bulkley power-law scaling occurs when the timescale of avalanches is comparable to the timescale between loading, and so stress is added to the system faster than avalanches can release it. What happens when avalanches begin to overlap in time? As the driving rate is increased, spatially distinct and largely noninteracting avalanches are nucleated faster than older avalanches conclude, as was shown by explicitly measuring the correlation length in athermal molecular dynamics [48]. Although we do not explicitly measure the correlation length or degree of spatial overlap in our system, we anticipate that a similar phenomenon takes hold as temperature is increased, with a regime of spatially distinct but temporally overlapping avalanches. This phase marks the beginning of HB scaling. At sufficiently high strain rates, the avalanches begin to increasingly overlap and interact, and it is no longer possible to individualize them as independent collective events.

Because our system is finite, the HB phase still has brief periods of quiescence with no plastic activity. Since we denote an “avalanche” as any period of plasticity bounded by periods of quiescence (of at least 3τ), we will be lumping together spatially distinct, but temporally overlapping avalanches. We can detect the onset of this behavior and consequently test our derived scaling laws for the onset of temporal avalanche overlap by considering the ratio of timescales $\langle t_{\text{load}} \rangle / \langle t \rangle_{\text{av}}$. As avalanches temporally overlap more and more, the durations between avalanches should become exponentially shorter and rarer, as can be seen in Fig. 4. It is clear that there is a temperature dependence in these curves, but also that for low temperatures, the results are identical. This is consistent with our phase diagram in Fig. 1, where avalanche overlap starts at fixed $\dot{x}_{\text{overlap}}[T < T_{\text{overlap}}(L)] \sim L^{-d/(1+\theta)}$ for low temperatures [Eq. (11)] and at $\dot{x}_{\text{overlap}}[T > T_{\text{overlap}}(L)] \sim L^{-d} T^{-\theta/\alpha}$ for high temperatures [Eq. (14)]. We can capture both scaling behaviors, and their dependence on system size, with the phenomenological scaling function,

$$\tau \dot{x}_{\text{overlap}}(T, L) \sim L^{-d/(\theta+1)} [1 + (T/T_{\text{overlap}})^{\theta/\alpha}]^{-1/s}, \quad (19)$$

which is characterized by a phenomenological sharpness parameter s (which we here take to be 2), and for the overlap

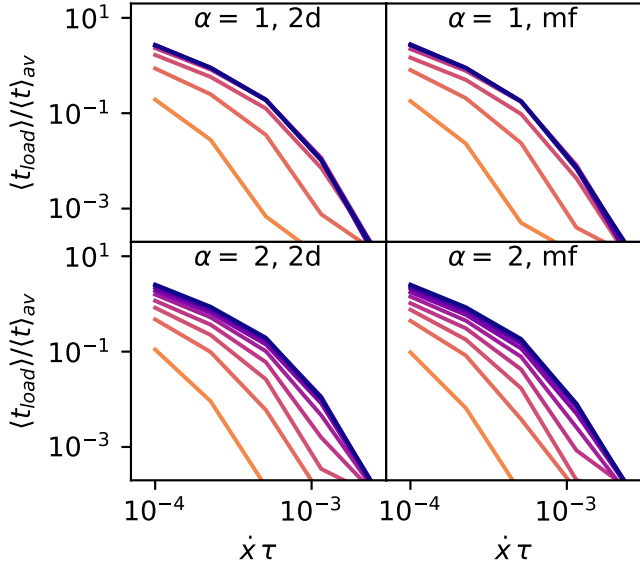


FIG. 4. Degree of avalanche overlap, as measured by the ratio of the waiting time and the average avalanche duration, for $L = 64$. Lighter colors are hotter temperatures.

temperature $T_{\text{overlap}} = CL^{-d\alpha/(1+\theta)}$, where C is an arbitrary constant prefactor [Eq. (15)]. We find that $C \approx 2$ for $\alpha = 1$ and $C \approx 20$ for $\alpha = 2$ produces an effective collapse for simulations with varying temperature, driving rate, and system size in Fig. 5. This confirms our scaling prediction for the onset of avalanche overlap, in both thermal and athermal regimes, and for the finite-size dependence of $T_{\text{overlap}}(L)$.

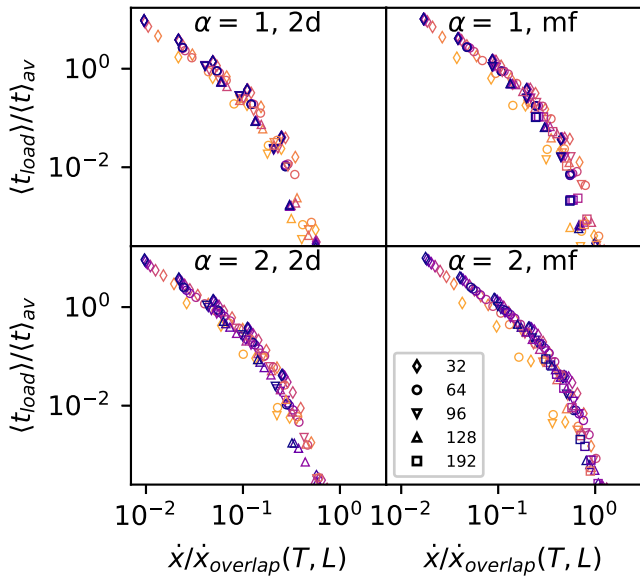


FIG. 5. Finite-size scaling collapse for the avalanche overlap parameter, for simulations with different temperatures (lighter colors show higher temperatures) and system sizes indicated by marker shape.

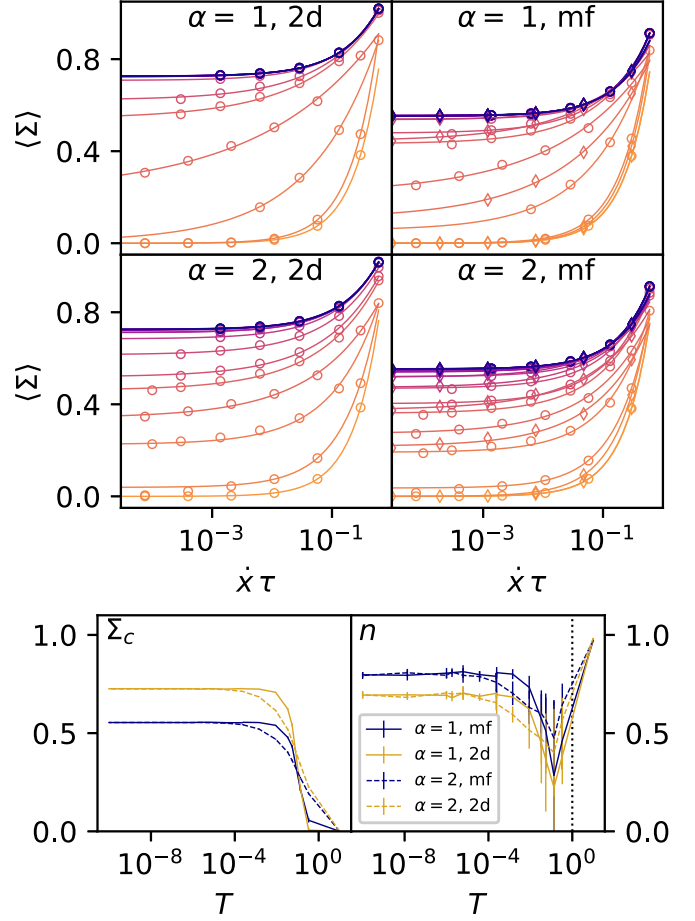


FIG. 6. Rheology data with Herschel-Bulkley fits for $L = 64$ (circles) and $L = 256$ (diamonds), allowing both exponent n and the temperature-dependent stress plateau $\Sigma_c(T)$ to vary. T varies from 10^{-10} to 3×10^{-1} . Bottom: fitted Σ_c and n values vary with temperature.

C. Rheology transition across $\dot{\gamma}_c(T)$

For strain rates above the avalanche-overlap threshold, the Herschel-Bulkley law $\dot{\gamma} \sim [\langle \Sigma \rangle - \Sigma_c(T)]^n$ is a reasonable fit to our data (cf. Fig. 6). We observe that at high-strain rates, stress tends towards the athermal value. However, simulations above a certain temperature show a decrease in the fitted flow stress and in the rheological exponent n (Fig. 6). At still higher temperatures ($T > 1$), the rheological exponent tends to $n = 1$ as would be expected for a Newtonian fluid. In general, there are minimal system-size effects in $\langle \Sigma \rangle$.

That the rheological exponent changes with n should not surprise experimentalists, where temperature-dependent viscosity effects have been seen to alter the rheological exponent [33]. However, since the exponent $1/n = \beta$ has been proposed to scale as $\beta = 1 + z/(d - d_f)$ (relating the flow exponent β to the dynamical exponent z and fractal dimension d_f) [49], naively this would suggest that the avalanche critical exponents would continuously vary with temperature. However, as we show below, this effect can be simply understood as fitting through two exponents operating in different regimes.

To expose this effect, in Fig. 7 we consider the stress rise above the flow stress $\Sigma_c(T)$ and divide out the AQS

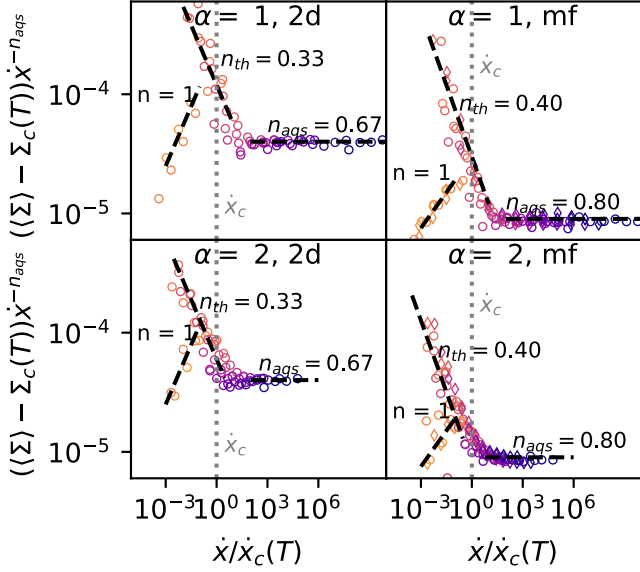


FIG. 7. Rheology data, rescaled to exhibit a change in the Herschel-Bulkley exponent n for $\dot{x} > \dot{x}_c(T) \sim \frac{1}{\tau} T^{1/\alpha}$. The AQS limit for n_{AQS} is included in the rescaling to make the transition to the thermal value n_{th} more evident. Simulations at $T = 10$ in the molten phase (brightest orange) obey $n = 1$ scaling.

Herschel-Bulkley exponent n_{AQS} . Although the decrease in n appears to be gradual in Fig. 6, our data in Fig. 7 show that the transition is actually sharp: there is a thermal and an athermal n exponent. Temperature effects seem to approximately halve the observed Herschel-Bulkley exponent n . By studying the stress rise above $\Sigma_c(T)$, we find that the athermal value n_{AQS} dominates when $\dot{x} > \dot{x}_c$ (cf. Fig. 7). The apparent intermediate values of n in Fig. 6 are a result of fitting through both regimes. We find the typical 2D AQS value for the Herschel-Bulkley exponent in EPMs ($n \approx 2/3$ [12]). We note that in experiments, $n \in [0.4, 1]$ have been reported, and indeed n can vary systematically in response to temperature [33] or pH [50].

At very high T , the system melts into a Newtonian fluid and the stress scales simply as $\langle \Sigma \rangle \sim \tau \dot{x}$, i.e., $n = 1$.

V. THERMALLY TRUNCATED AVALANCHES

We have provided numerical evidence for the existence of different dynamic phases in our phase diagram. Now we seek to clarify the effect of temperature on the well-defined avalanches in region 3 of the phase diagram. There, temperature is high enough to overcome finite-size effects (in contrast to region 2), while remaining low enough that (with sufficiently slow driving) avalanches do not overlap (in contrast to region 4). In this case, as we showed previously, the average avalanche size scales as $\langle S \rangle \sim T^{-\theta/\alpha}$ and, owing to Eq. (18), we have that $S_c \sim T^{-\theta/[\alpha(2-\tau)]}$, with minimal system-size dependence.

However, if driving rates are lowered far below the Herschel-Bulkley onset, a thermal softening of the material occurs as even nominally stable sites above $x_c = T^{1/\alpha}$ can be activated and the mean flow stress $\langle \Sigma \rangle$ is depressed by temperature (see Fig. 6). At extremely low strain rates

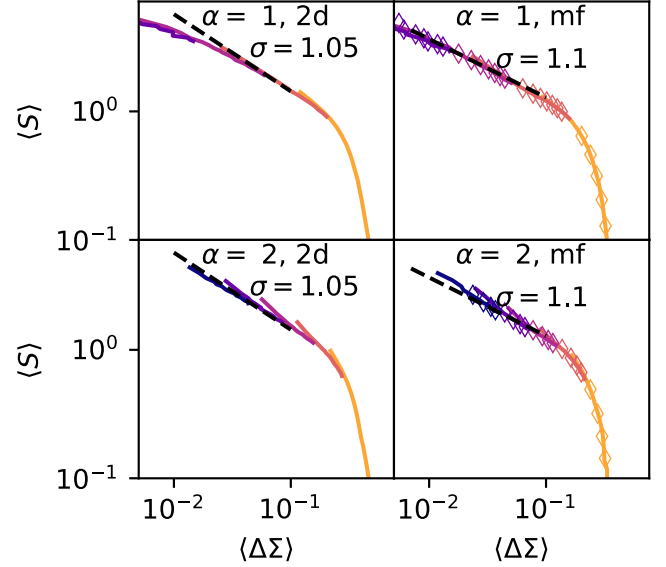


FIG. 8. Power-law scaling for mean avalanche size with the stress gap created at extremely slow driving. Power-law fit uses $\tau = 3/2$ for mean-field (MF) data and $\tau \approx 1.37$ for 2D data. Scaling of dashed lines is set by Eq. (20), with indicated fit values of σ . Lines are $L = 64$, with diamonds indicating results for $L = 256$.

[in our data, with $\dot{x} \in (10^{-22}, 10^{-9})$], there is additional softening below the apparent plateau present in Fig. 6. To obtain a representative sample of avalanches for systems strained this slowly requires simulating extremely long waiting times between avalanches, which we are able to access by analytically inverting the waiting time distribution, as described in Appendix A 1. This softening introduces a stress gap, $\Delta \Sigma(T, \dot{x}) = \Sigma_{\text{AQS}} - \langle \Sigma \rangle(T, \dot{x})$ [where $\Sigma_{\text{AQS}} \equiv \lim_{\dot{\gamma} \rightarrow 0^+} \langle \Sigma \rangle(T = 0, \dot{\gamma}) = \Sigma_c(T = 0)$], which means that on average, there is less energy available for avalanches to propagate.

The stress gap introduces a power-law scaling in avalanche size cutoff, $S_c \sim |\Delta \Sigma|^{-1/\sigma}$, with a new exponent $1/\sigma$. This exponent has been measured in EPM by fixing the stress of the system with $\Sigma < \Sigma_{\text{AQS}}$ and artificially triggering an avalanche by kicking a random site [17] or by measuring avalanches in the approach to steady-state flow [51]. However, with the temperature-dependent stress gap entering, $1/\sigma$ can be probed naturally, by considering the mean-avalanche size for simulations at slow driving, where Eq. (18) implies

$$\langle S \rangle \sim |\Delta \Sigma|^{(\tau-2)/\sigma}. \quad (20)$$

Our data in Fig. 8 are consistent with $1/\sigma \approx 0.91$, although the data are limited to less than a decade for $\alpha = 2$. This value of $1/\sigma$ is higher than that reported in previous reports. Here, however, the exponent has been measured in a strain-controlled simulation, while previous measurements were in stress-controlled simulations. In Ref. [17], where stress was fixed below the flow stress and random sites were kicked, $1/\sigma \approx 0.51$, while in Ref. [51], where avalanches were measured in the transient regime as the system was loaded to its critical point, $1/\sigma \approx 0.59$ [which we infer from the scaling of Eq. (20) and their mean avalanche size data]. Our explanation for this discrepancy is the following: avalanche propagation

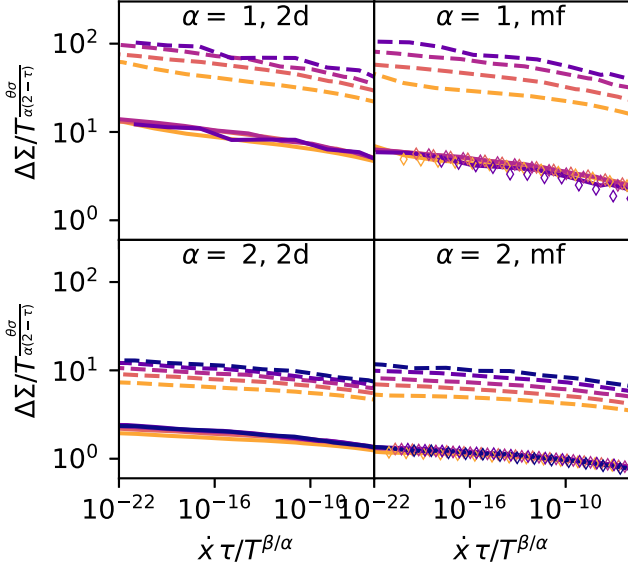


FIG. 9. The stress-softening effect, collapsed according to our proposed scaling $\Delta\Sigma \sim T^{\frac{\theta\sigma}{\alpha(2-\tau)}}$ (solid lines) and according to the previously proposed scaling $\Delta\Sigma \sim T^{1/\alpha}$ (dashed lines) for both the shuffled-kernel and 2D simulations. For clarity, the dashed lines have been shifted vertically by a factor of 3. All simulations are $L = 64$, and $T \in (10^{-4}, 3 \times 10^{-2})$; see Table II for the exponent used in collapse.

depends on the number of sites with small residual stress and on correlations between sites. We propose that the exponent $1/\sigma$ therefore depends on how the stress gap $\Delta\Sigma$ is established. In our case, sites with $x < x_c(T)$ (and for low driving, sites $x \approx x_c$) are suppressed. In the above-mentioned works, the $p(x)$ distribution evolved with the stress gap, with substantially lower values of θ reported.

In any case, if we combine Eq. (16) and Eq. (20), we obtain

$$\Sigma_{\text{AQS}} - \langle \Sigma \rangle(T, \dot{\gamma}) = \Delta\Sigma \sim T^{\theta\sigma/[\alpha(2-\tau)]}, \quad (21)$$

which collapses our low-strain rate stress-gap data (cf. Fig. 9). This scaling argument does not account for strain-rate effects, but we find that these are relatively modest over more than 10 decades of strain-rate data.

In prior work on thermally activated flow in amorphous solids, the characteristic stress scale was identified as $\Delta\Sigma \sim T^{1/\alpha}$, per Eq. (2), and the strain rate is scaled by the thermal yielding exponent $\psi = \beta/\alpha$ as $\dot{\gamma}/T^{\beta/\alpha}$ [35,36]. We find that this scaling does not effectively collapse our low strain-rate

simulations (see the dashed lines in Fig. 9). We speculate that the scaling $\Delta\Sigma \sim T^{\theta\sigma/[\alpha(2-\tau)]}$ was not previously noted because $\theta\sigma/[\alpha(2-\tau)] \approx 0.8/\alpha$ is not so dissimilar from $1/\alpha$. The difference in scaling is only obvious when excluding the data from the fast-driving Herschel-Bulkley regime (where the $T^{1/\alpha}$ scaling applies)—if the data from the fast-driving regime is included, this gap in scaling is visually compressed.

Why do different stress scales appear in slow- and fast-driving regimes? We propose that in the case of slow driving, with nonoverlapping avalanches, the appropriate stress scale is set by the typical stress dissipated by a single avalanche. This leads to the scaling in Eq. (21). When avalanches begin to overlap, the pertinent stress scale becomes the stress dissipated by individual STs, for which the relevant stress scale is $x_c \sim T^{1/\alpha}$. Of course, it is also possible that this alteration in scaling is linked to our use of a strain-controlled driving protocol, while previous simulations used stress-controlled loading.

VI. CONCLUSIONS

We have derived a schematic dynamic phase diagram for sheared amorphous solids at finite temperatures by comparing the main timescales of the problem. Using EPM simulations, we have provided numerical evidence for these phase lines, by varying the exponent α , and by use of a shuffled kernel, the exponent θ . The main phase lines dictate whether thermal activation occurs and whether avalanches overlap. Avalanche overlap has strong finite-size effects, while the threshold for thermal effects is size independent. In the infinite system-size limit, the strict AQS critical point occurs only for $T = 0$ and $\dot{x} = 0$. Avalanches can be truncated by either finite-size effects or by temperature, and we have derived appropriate scaling arguments for both cases.

Our simulations complement prior stress-controlled work, and in agreement with that work find that $x_c \sim \Delta\Sigma \sim |\langle \Sigma \rangle - \Sigma_{\text{AQS}}| \sim T^{1/\alpha}$ is the appropriate stress scale when avalanches overlap [35,36]. When avalanches do not overlap, i.e., before Herschel-Bulkley flow onset in the low-strain rate limit, thermal effects soften the material and introduce a new temperature-dependent stress gap. Using scaling arguments, we have linked that stress gap to the stress dissipated by avalanches, finding $\Delta\Sigma \sim \Sigma_{\text{AQS}} - \langle \Sigma \rangle T^{(\theta\sigma)/[\alpha(2-\tau)]}$. Intriguingly, this brings the AQS $1/\sigma$ exponent, which is normally only exposed by stress-controlled simulations, into the thermal problem. Since we arrived at that scaling using generic scaling arguments, it should also hold in stress-controlled simulations.

One avenue that this work does not touch on is aging and thermal history dependence. We use a fixed Weibull distribution for site yield thresholds σ_{th} , but the threshold distribution has temperature and history dependence [52,53]. To what extent this affects critical behavior beyond the ductile-brittle transition has not been elucidated.

Another aspect that deserves further study is why the thermal Herschel-Bulkley exponent takes the value it does. Can this be linked by appropriate scaling arguments to the other critical exponents, as is done in the athermal case [12,49]? An accurate space-time exponent z would need to be measured, along with the correlation length exponent ν

TABLE II. Numerically observed exponents for the thermal EPM model, with \pm errors representing acceptable fit ranges.

Exponent	Definition	Value (2D)	Value (MF)
τ	$p(S) \sim s^{-\tau} G(S/S_c)$	1.37 ± 0.07	1.5 ± 0.05
σ	$S_c \sim (\Delta\Sigma)^{-1/\sigma}$	1.05 ± 0.08	1.1 ± 0.06
θ	$p(x) \sim x^\theta$	0.52 ± 0.05	0.35 ± 0.03
n (athermal)	$\Sigma = \Sigma_c + C\dot{\gamma}^n$	0.67 ± 0.02	0.8 ± 0.02
n (thermal)	$\Sigma = \Sigma_c(T) + C\dot{\gamma}^n$	0.33 ± 0.06	0.4 ± 0.04
n (molten)	$\Sigma = \tau\mu\dot{\gamma}^n$	1 ± 0.01	1 ± 0.01

(or its thermal equivalent). We predict a decrease in the correlation length throughout regime 3, where temperature effects truncate avalanche propagation. Although we do not attempt to separate temporally overlapping but spatially distinct avalanches, as might be possible for low driving rates, temperatures, and for large systems in the HB regime, we expect correlation lengths will continue to decrease with temperature in the HB regime.

An interesting observation is that both the thermal and athermal Herschel-Bulkley exponent differ when the kernel is shuffled and correlations between sites are destroyed. This highlights that although the correlation length in the thermal regime is likely shorter ranged, collective events are still playing a role. With shuffled-kernel simulations, we notice that the flow stress is much lower than in full 2D simulations. This indicates that systems with correlated noise evolve to rather different steady states. Does this in turn produce different types of mechanical noise, beyond just that expected by having linelike plastic events? If so, is it enough to simply plug in the different noise distributions at the mean-field level (in the spirit of [16,20]) to explain the observed Herschel-Bulkley exponent for the shuffled kernel? Would this approach extend into the thermal regime with n_{th} ? Additionally, our observation that the shuffling of the kernel alters the θ and n exponents suggests that the correlations that can build up between sites in low-dimension matter. By contrast, Ref. [17] found that critical exponents did not change between $d = 2$ and $d = 3$.

ACKNOWLEDGMENTS

This research was undertaken thanks, in part, to funding from the Canada First Research Excellence Fund, Quantum Materials and Future Technologies Program. D.K. thanks Natural Sciences and Engineering Research Council of Canada (NSERC) for financial support through a CGS-D scholarship.

APPENDIX A: IMPLEMENTATION DETAILS

1. Loading times

Sites liquify by thermal activations at rate $\lambda(x)$ or immediately at $x = 0$. To simulate the dynamics of our systems, we essentially need to work out which site i will fail next and at what time δt (while correctly accounting for loaded stress \dot{x}). Once the next site to liquify is known, stresses propagated from that site can be worked out using the finite-element solver, and stress can be relaxed at the failing site. During the time increment δt , all sites have their stresses increased by $\dot{x} \delta t$ and any propagated stresses or relaxations are scaled by a factor of $\sim \exp[-\delta t/\tau]$ applied.

Working out the inter-event period δt and site i is relatively trivial for fixed stress simulations between avalanches, where activations happen at fixed rate $\lambda(x)$. Since activations are independent Poisson processes, with an exponentially decaying waiting time probability distribution function $p(t) = \lambda(x_i)e^{-\lambda(x_i)t}$, for a system with $N = L^d$ sites one could sample N random numbers $\{R_i \in [0, 1)\}$ and find the next activation time for each site by inverting the cumulative distribution function for the exponentially distributed waiting times, so that each site is assigned a time: $t_i = \frac{-1}{\lambda(x_i)} \ln(1 - R_i)$. By

finding the i with the smallest t_i , one has found the first site to yield, and the appropriate interval $\delta t = t_i$. This naive scheme could obviously be improved by using a global rate, $\lambda = \sum_i \lambda(x_i)$, and choosing a site i at random with weight $\lambda(x_i)$, which reduces the problem to requiring only two random numbers, instead of N .

In our system, because σ_i evolves in time between ST events as

$$\sigma_i(t) = \sigma_{i,0} + \dot{x}t + \sigma_i^{\text{nonlocal}}(1 - e^{-t/\tau}), \quad (\text{A1})$$

where $\sigma_i^{\text{nonlocal}}$ are the stresses propagating from liquified sites to site i , the Poisson rates $\lambda(x_i)$ are not constant. We follow the “naive” approach, but generalized to inhomogeneous Poisson processes, for each site sampling a random number $R_i \in [0, 1)$, and solving for t_i as

$$R_i = P(t < t_i) = \exp \left\{ - \int_0^{t_i} \lambda[x_i(t)] dt \right\}. \quad (\text{A2})$$

As before, once we have a t_i for each site, we pick the lowest t_i for δt and liquify site i . In practice, we solve Eq. (A2) in two ways: (i) after all $\sigma_i^{\text{nonlocal}}$ have decayed by 25τ and are negligible, $\sigma_i(t)$ are linear in time, and Eq. (A2) can be solved and inverted analytically for $\alpha = 1$ and $\alpha = 2$; (ii) when $\sigma_i(t)$ are nonlinear, we solve Eq. (A2) numerically by constructing and solving a related initial value problem (IVP).

For the analytical case, using $\lambda(x) = \frac{1}{\tau} \exp(-x^\alpha/T)$, we restrict ourselves to $\alpha = 1$ and $\alpha = 2$. For $\alpha = 1$, with $x(t) = \sigma_{\text{th}} - (\sigma_0 - \dot{x}t)$ (suppressing the subscripts for brevity), we have

$$\int_0^{t_i} \lambda[x(t)] dt = \frac{T}{\dot{x}\tau} e^{-(\sigma_{\text{th}} - \sigma_0)/T} (e^{t_i \dot{x}/T} - 1).$$

Since $R_i = 1 - e^{\int_0^{t_i} \lambda[x_i(t)] dt}$, we can solve for t_i as

$$t_i = \frac{\sigma_{\text{th}} - \sigma_0}{\dot{x}} + \frac{T}{\dot{x}} \ln \left[e^{-(\sigma_{\text{th}} - \sigma_0)/T} + \ln(1 - R_i) \frac{\tau \dot{x}}{T} \right],$$

where we can recognize the first term as the mechanical yielding timescale $(\sigma_{\text{th}} - \sigma_0)/\dot{x} = x/\mu\dot{\gamma}$, and the second as a temperature-dependent stochastic correction that can reduce the time to yield. The $\alpha = 2$ case is similar and gives

$$t_i = + \frac{\sigma_{\text{th}} - \sigma_0}{\dot{x}} - \frac{\sqrt{T}}{\dot{x}} \text{erf}^{-1} \left[\text{erf} \left(\frac{\sigma_{\text{th}} - \sigma_0}{\sqrt{T}} \right) + \frac{2\dot{x}\tau}{\sqrt{\pi T}} \ln(1 - R_i) \right].$$

These analytical equations are used between avalanches for potentially very long loading periods. This avoids a potentially expensive numerical integration at each site, since a small time step (comparable to τ) is necessary to avoid missing the thermal activation of a site (since a site approaching $x \approx x_c = T^{1/\alpha}$ activates, on average, on a timescale $\approx \tau$). In practice, since $x \equiv \sigma_{\text{th}} - |\sigma|$, we also consider the case $x(t) = \sigma_{\text{th}} + \sigma_0 - \dot{x}t$ to catch the (rare) events in which negatively stressed sites yield thermally. Additionally, these equations are prone to numerical under- and overflows, so care must be taken when implementing these equations to deal with potential numerical pitfalls.

The numerical description is conceptually simpler, though more computationally expensive. To solve Eq. (A2)

numerically, consider the obviously related function $R(t) = \exp\{-\int_0^t \lambda[x_i(t')]dt'\}$, for which $R(t_i) = R_i$ is our desired solution. $R(t)$ obeys the following differential equation:

$$\frac{dR}{dt} = [1 - R(t)]\lambda[x_i(t)], \quad (\text{A3})$$

for which the IVP $R(t=0) = 0$ and $R(t_i) = R_i$ (where R_i is still randomly drawn from $[0,1)$) has a unique solution. We use SCIPY's solve-ivp routine [54] to integrate these equations for all sites simultaneously—halting when either $R(t_i) = R_i$ for a site or $x_i = 0$ for a site. As in the analytical case, we consider both cases of $x_i = \sigma_{th} \pm \sigma_i(t)$, allowing for a site to yield because it is stressed too far in either direction. Since the Eshelby-like stress propagator has both positive and negative kicks, sites frequently fail in either direction during an avalanche (though they are biased to fail in the forward loading direction).

2. Stress propagator and shuffled kernel

When sites liquify, they reduce their stress and redistribute stresses elsewhere in the system. We use the finite-element method on a regular triangular mesh to determine the stress propagation between sites. Each square site in the system consists of four finite-element triangles terminating in a central vertex. We use first-order Lagrange elements for the displacement field \underline{u} [with simple-shear fixed boundary conditions $\underline{u}[(x, y) \in \partial\Omega] = (\gamma y, 0)^T$], and zeroth-order discontinuous Galerkin elements to represent the stresses, strains, and plastic strains on the plaquettes. We relate the total strain to the displacement as

$$\underline{\gamma} = \frac{1}{2}[(\nabla \underline{u}) + (\nabla \underline{u})^T], \quad (\text{A4})$$

and decompose the strain tensor into plastic (stress-free) and elastic parts as $\underline{\gamma} = \underline{\gamma}_{pl} + \underline{\gamma}_{el}$. The elastic strain contributes to the tensorial stress as

$$\underline{\sigma} = 2\mu\underline{\gamma}_{el} + \lambda\text{tr}(\underline{\gamma}_{el})\mathbb{1}, \quad (\text{A5})$$

where, for our simulations, we use $\mu = 1$ and $\lambda = \frac{1}{2}$. The local stress σ_i at a site i is the average $\underline{\sigma}_{xy}$ component of the stress over the square cell. To work out the long-time stress field from a liquified site, we increment the plastic strain at that site (equally distributed over all triangles) by the stress at the site. We then solve the elastic equations and find the stress increments $\delta\sigma_{ij}$ at all sites in the system. For each site j in the system, we then set $\sigma_j^{\text{nonlocal}} \rightarrow \sigma_j^{\text{nonlocal}} + \delta\sigma_{ij}$, so that this stress increment is applied exponentially over the next several time units τ .

For the shuffled-kernel simulations, we first identify a central site i in the system [e.g., for $L = 32$ at $(x, y) = (15, 15)$]. We then apply a nominal plastic strain of magnitude 1 and work out the resulting $\delta\sigma_{ij}$ at all sites. The resulting set of $N - 1$ stress increments $\{\delta\sigma_{ij}\}$ is then stored for later use, so that the expensive finite-element calculation is not repeated throughout the mean-field simulations. When a site k in the shuffled-kernel simulation fails, all sites receive a stress increment $\sigma_j^{\text{nonlocal}} \rightarrow \sigma_j^{\text{nonlocal}} + \sigma_k\delta\sigma_{ij'}$, where the j' are drawn

without replacement from $\{1, 2, \dots, i-1, i+1, \dots, N\}$. The failing site of course receives the stress increment $\sigma_k^{\text{nonlocal}} = \sigma_k\delta\sigma_{ii} \approx -\sigma_k$. In this way, the stress increments initially calculated for a central site are shuffled for the nonfailing site and scaled according to the stress at the failing site, and the failing site relaxes in accordance with its stress.

APPENDIX B: $P(X)$ FORM

For simulations with well-defined avalanches, $p(x)$ can be sampled immediately after each avalanche. The distribution of $p(x)$ then can be used to predict the loading time before the next avalanche. For simulations with $\dot{x} < \dot{x}_c(T)$, we find that $p(x)$ takes the form of a power law with an exponential cutoff at $x < x_c = T^{1/\alpha}$, as can be seen in Fig. 10. For simulations with a higher-driving rate, however, there is a system-size-dependent and velocity-dependent plateau (Fig. 10). We expect the velocity-dependent plateau to occur at $x \approx \tau \dot{x}$, while the system-size-dependent terminal plateau should scale as $x \sim L^{-d}$ [44,46]. We approximate the plateau

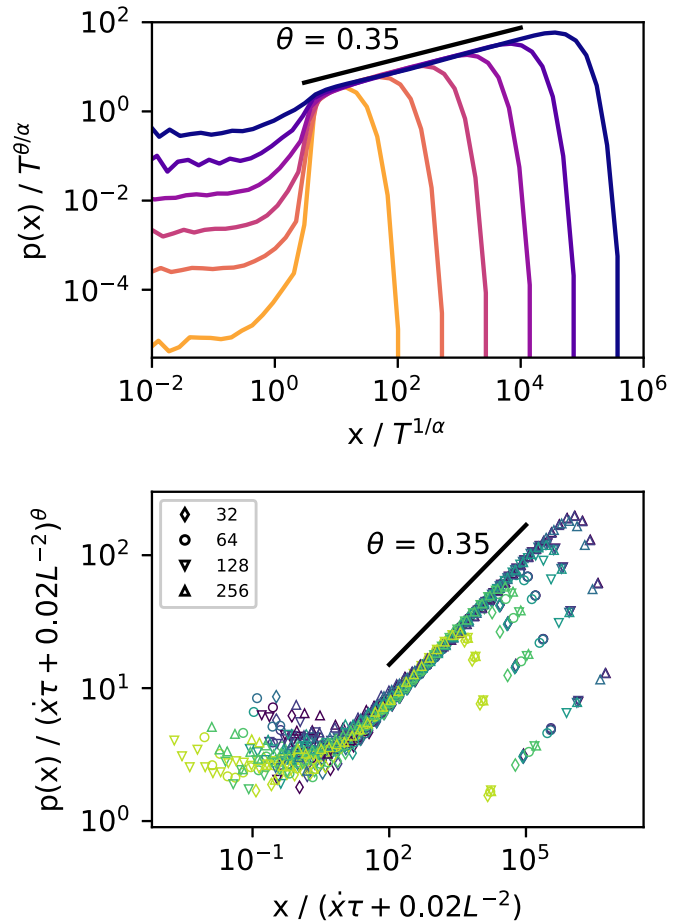


FIG. 10. The residual stress distributions of shuffled-kernel simulations ($\theta = 0.35$), rescaled by characteristic scales set by temperature, velocity, or finite-size effects. Top: $p(x)$ for simulations with different values of T (lighter colors have higher T) and $L = 256$, rescaled by $x_c = T^{1/\alpha}$ for low velocities. Bottom: $p(x)$ for simulations with different values of v (lighter colors have higher strain rate) and L (indicated by symbol), rescaled by $x_p = (\tau\dot{x} + 0.02L^{-2})$.

as occurring at $x_p = (\tau\dot{x} + 0.02L^{-2})$, which effectively collapses the plateau onset in Fig. 10.

APPENDIX C: EXPONENTS AND SCALING RELATIONS

When avalanches are well defined, the maximum avalanche size S_c is set by either temperature effects or

finite-size effects. In the case of finite-size effects, the fractal dimension of avalanches enters, with $S_c \sim L^{d_f}$. Our scaling description based on a simple truncated power law for $p(x)$ finds that $d_f = d/[(\theta + 1)(2 - \tau)]$ in the athermal limit. When temperature effects are larger than finite-size effects, the maximum avalanche size scales as $S_c(T) \sim T^{-\theta/[\alpha(2-\tau)]}$ or as $S_c \sim (\Delta\Sigma)^{-1/\sigma}$.

-
- [1] D. Bonn, M. M. Denn, L. Berthier, T. Divoux, and S. Manneville, *Rev. Mod. Phys.* **89**, 035005 (2017).
 - [2] C. A. Schuh, T. C. Hufnagel, and U. Ramamurty, *Acta Mater.* **55**, 4067 (2007).
 - [3] M. L. Manning, E. G. Daub, J. S. Langer, and J. M. Carlson, *Phys. Rev. E* **79**, 016110 (2009).
 - [4] S. M. Fielding, *Rep. Prog. Phys.* **77**, 102601 (2014).
 - [5] H. J. Barlow, J. O. Cochran, and S. M. Fielding, *Phys. Rev. Lett.* **125**, 168003 (2020).
 - [6] A. S. Argon, *Acta Metallurg.* **27**, 47 (1979).
 - [7] A. S. Argon and H. Y. Kuo, *Mater. Sci. Eng.* **39**, 101 (1979).
 - [8] C. E. Maloney and A. Lemaître, *Phys. Rev. E* **74**, 016118 (2006).
 - [9] A. Nicolas, F. Puosi, H. Mizuno, and J.-L. Barrat, *J. Mech. Phys. Solids* **78**, 333 (2015).
 - [10] T. Albaret, A. Tanguy, F. Boioli, and D. Rodney, *Phys. Rev. E* **93**, 053002 (2016).
 - [11] A. Nicolas and J. Rottler, *Phys. Rev. E* **97**, 063002 (2018).
 - [12] J. Lin, E. Lerner, A. Rosso, and M. Wyart, *Proc. Natl. Acad. Sci.* **111**, 14382 (2014).
 - [13] S. Sandfeld, Z. Budrikis, S. Zapperi, and D. F. Castellanos, *J. Stat. Mech.: Theory Expt.* (2015) P02011.
 - [14] E. A. Jagla, *Phys. Rev. E* **92**, 042135 (2015).
 - [15] C. Liu, E. E. Ferrero, F. Puosi, J.-L. Barrat, and K. Martens, *Phys. Rev. Lett.* **116**, 065501 (2016).
 - [16] J. Lin and M. Wyart, *Phys. Rev. X* **6**, 011005 (2016).
 - [17] Z. Budrikis, D. F. Castellanos, S. Sandfeld, M. Zaiser, and S. Zapperi, *Nat. Commun.* **8**, 15928 (2017).
 - [18] I. Fernández Aguirre and E. A. Jagla, *Phys. Rev. E* **98**, 013002 (2018).
 - [19] E. E. Ferrero and E. A. Jagla, *Soft Matter* **15**, 9041 (2019).
 - [20] E. E. Ferrero and E. A. Jagla, *J. Phys.: Condens. Matter* **33**, 124001 (2021).
 - [21] J. Lin, A. Saade, E. Lerner, A. Rosso, and M. Wyart, *Europhys. Lett.* **105**, 26003 (2014).
 - [22] M. Le Goff, E. Bertin, and K. Martens, *Phys. Rev. Lett.* **123**, 108003 (2019).
 - [23] K. Karimi, E. E. Ferrero, and J.-L. Barrat, *Phys. Rev. E* **95**, 013003 (2017).
 - [24] K. M. Salerno, C. E. Maloney, and M. O. Robbins, *Phys. Rev. Lett.* **109**, 105703 (2012).
 - [25] A. Nicolas, J.-L. Barrat, and J. Rottler, *Phys. Rev. Lett.* **116**, 058303 (2016).
 - [26] K. M. Salerno and M. O. Robbins, *Phys. Rev. E* **88**, 062206 (2013).
 - [27] A. Nicolas, E. E. Ferrero, K. Martens, and J.-L. Barrat, *Rev. Mod. Phys.* **90**, 045006 (2018).
 - [28] E. R. Homer and C. A. Schuh, *Acta Mater.* **57**, 2823 (2009).
 - [29] Y. Shi and M. L. Falk, *Phys. Rev. Lett.* **95**, 095502 (2005).
 - [30] Y. Shi and M. L. Falk, *Phys. Rev. B* **73**, 214201 (2006).
 - [31] S. Karmakar, E. Lerner, I. Procaccia, and J. Zylberg, *Phys. Rev. E* **82**, 031301 (2010).
 - [32] L. Bécu, S. Manneville, and A. Colin, *Phys. Rev. Lett.* **96**, 138302 (2006).
 - [33] M. Caggioni, V. Trappe, and P. T. Spicer, *J. Rheol.* **64**, 413 (2020).
 - [34] J. Chattoraj, C. Caroli, and A. Lemaître, *Phys. Rev. Lett.* **105**, 266001 (2010).
 - [35] M. Popović, T. W. J. de Geus, W. Ji, and M. Wyart, *Phys. Rev. E* **104**, 025010 (2021).
 - [36] E. E. Ferrero, A. B. Kolton, and E. A. Jagla, *Phys. Rev. Mater.* **5**, 115602 (2021).
 - [37] M. Popović, T. W. J. de Geus, W. Ji, A. Rosso, and M. Wyart, *arXiv:2111.04061*.
 - [38] S. Bustingorry, A. B. Kolton, and T. Giamarchi, *Europhys. Lett.* **81**, 26005 (2008).
 - [39] C. E. Maloney and D. J. Lacks, *Phys. Rev. E* **73**, 061106 (2006).
 - [40] D. G. Truhlar, B. C. Garrett, and S. J. Klippenstein, *J. Phys. Chem.* **100**, 12771 (1996).
 - [41] A. Nicolas, J. Rottler, and J.-L. Barrat, *Eur. Phys. J. E* **37**, 50 (2014).
 - [42] C. Ruscher and J. Rottler, *Soft Matter* **16**, 8940 (2020).
 - [43] C. Liu, S. Dutta, P. Chaudhuri, and K. Martens, *Phys. Rev. Lett.* **126**, 138005 (2021).
 - [44] B. Tyukodi, D. Vandembroucq, and C. E. Maloney, *Phys. Rev. E* **100**, 043003 (2019).
 - [45] J. T. Parley, S. M. Fielding, and P. Sollich, *Phys. Fluids* **32**, 127104 (2020).
 - [46] D. Korchinski, C. Ruscher, and J. Rottler, *Phys. Rev. E* **104**, 034603 (2021).
 - [47] H. G. E. Hentschel, S. Karmakar, E. Lerner, and I. Procaccia, *Phys. Rev. Lett.* **104**, 025501 (2010).
 - [48] J. T. Clemmer, K. M. Salerno, and M. O. Robbins, *Phys. Rev. E* **103**, 042605 (2021).
 - [49] J. Lin and M. Wyart, *Phys. Rev. E* **97**, 012603 (2018).
 - [50] I. A. Gutowski, D. Lee, J. R. de Bruyn, and B. J. Frisken, *Rheol. Acta* **51**, 441 (2012).
 - [51] J. Lin, T. Gueudré, A. Rosso, and M. Wyart, *Phys. Rev. Lett.* **115**, 168001 (2015).
 - [52] S. Patinet, D. Vandembroucq, and M. L. Falk, *Phys. Rev. Lett.* **117**, 045501 (2016).
 - [53] A. Barbot, M. Lerbinger, A. Hernandez-Garcia, R. García-García, M. L. Falk, D. Vandembroucq, and S. Patinet, *Phys. Rev. E* **97**, 033001 (2018).
 - [54] P. Virtanen, R. Gommers, T. E. Oliphant, M. Haberland, T. Reddy, D. Cournapeau, E. Burovski, P. Peterson, W. Weckesser, J. Bright, S. J. van der Walt, M. Brett, J. Wilson, K. J. Millman, N. Mayorov, A. R. J. Nelson, E. Jones, R. Kern, E. Larson, C. J. Carey *et al.*, *Nat. Methods* **17**, 261 (2020).